

Morphological Image Processing of Bioceramic Foam

Sang-hun Lee^{1,*}

¹Department of Environmental Science, Keimyung University, Daegu 42601, Korea
(Received October 14, 2017; Revised November 20, 2017; Accepted November 22, 2017)

ABSTRACT

A new morphological image processing algorithm is proposed for automatically and non-destructively analyzing the cellular structure of planar-type bioceramic foam using an optical microscope. With an abundant cell density, the cell structure can differentiate high cell volume fraction, high degree of interconnection to neighboring cells, and variable cell sizes. Our primary focus was to identify whether the distribution in cell sizes could be reliably measured by automatically delineating cell boundaries on the basis of a difference in the optical reflection of the cell and strut. There should be no mechanical or chemical pretreatment needed to enhance their visibility. Under this condition, an appropriate cell-marking process is required to discriminate each cell with a variation in light intensity. However, it is not possible to apply this procedure using a conventional microscopic technique. Therefore, a novel boundary construction operation was designed that can describe boundaries based not only on cell shapes but also on the light intensity of cells. The results of the operation enable us to quantify important characteristics, such as cell size distribution and perimeter size. The proposed method has advantages over the conventional segmentation (i.e., watershed) method in quantifying cell structures with larger cells; however, a longer computing time is required.

Key words : Bioceramic foam, Cellular structure, Image processing, Microscope

Introduction

Interest in bioceramic foams is increasing because of their wide applicability in many fields such as microbial fermentation, food processing, and medical applications [1,2]. The cellular structure consists of an interconnected network of solid walls called struts. Its cellular characteristics significantly influence its applications [3]. There are many methods to analyze the characteristics of these foams; however, image analysis is accepted as the one of the most convenient techniques for description of cellular structures [4]. For example, a recent study by Tong et al. described the dry foam generated in a bubbling (i.e., flotation) process using image analysis methods

[5]. Ou et al. resolved the cellular SiC foams with X-ray tomography using image analysis [6]. Both these studies developed adequate image processing or reconstruction methods for enhancing the significant features prior to quantifying characterization. In spite of these efforts, De Pascalis et al. indicated that no effective reconstruction algorithm for foam structures could yet detect the shapes of cellular foam structures without an expensive high-resolution 3D imaging technology, incurring high cost and requiring operational expertise [7].

Therefore, in this study, using conventional microscopy, an image processing algorithm was designed to analyze cellular structures from a gray image of bioceramic foam surfaces. This includes an original automatic boundary construction method, which is the most challenging part in this study. The bioceramic foam, casted using a powder processing technique, possesses a high cell volume fraction (porosity over

* Correspondence should be addressed to Sang-hun Lee, Department of Environmental Science, Keimyung University, 1095 Dalgubeol-daero, Daegu 42601, Korea. Tel: +82-53-580-5912, Fax: +82-53-580-6286, E-mail: shlee73@kmu.ac.kr

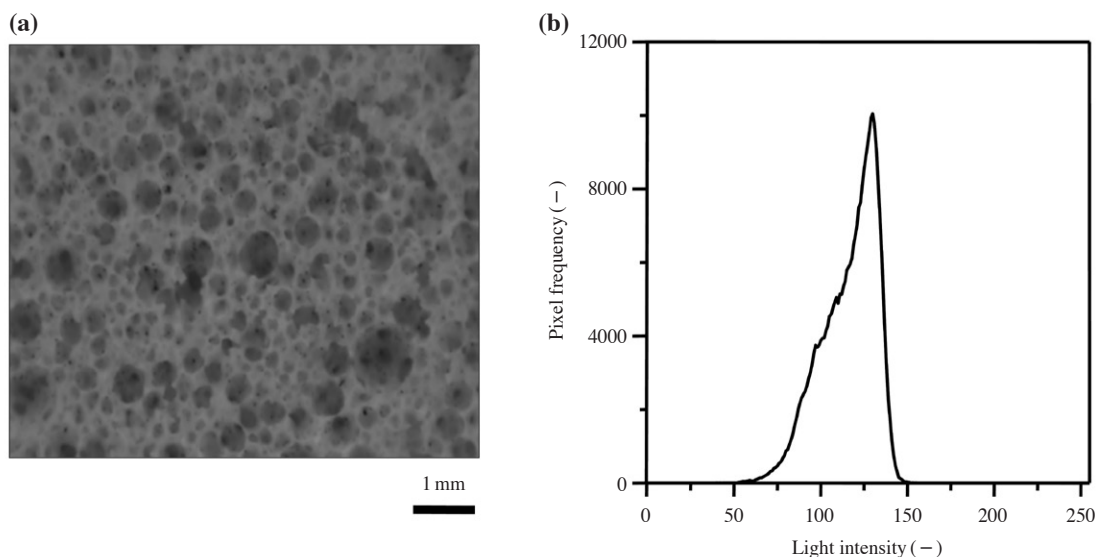


Fig. 1. (a) The sample image to be segmented (b) Its light (brightness) intensity histogram.

70%), a large degree of interconnection to neighboring cells, and variable cell sizes ($10\sim1000\ \mu\text{m}$); a typical image is shown in Fig. 1. An open-cellular surface consists of three parts: cells, struts, and cell windows, which are the small interconnections between cells. Some of the cell windows were detected as dark holes in the image because of low light reflection. Therefore, the light intensity from these was lower than from the cell or strut part. In general, the light intensity from the cell was lower than that from a strut, but higher than that from a cell window. Unfortunately, in such images, the boundaries are not clearly identifiable; furthermore, the cell windows with an irregular spatial distribution also hide their boundaries. The obvious distinction between both these kinds of boundaries seemed difficult to segment using simple image processing methods. The surface in the image contains high roughness and an irregular spatial distribution of cells and cell windows. For example, the simplest task in boundary detection or construction is the threshold operation based on global brightness or its gradient in each pattern [8-11]. However, it was difficult to detect the structure in Fig. 1 using simple segmentation. Therefore, in this study, an image algorithm was developed that can detect and segment each cell using more sophisticated image operations.

To segment the features, parts of the boundaries were extracted using a threshold operation after image acquisition and pre-processing for noise reduction. Next, using the extracted boundaries, each cell was marked. Finally, as the most significant and strenuous step, other boundaries were delineated.

This used not only common tools such as threshold and skeleton operations, but also the so-called binary reconstruction to correct the faults from closely bounded objects and gray scale reconstruction to mark the cell [12,13]. The results of these segmentation studies were that, using the abovementioned method, we can quantify the important characteristic items such as cell size and perimeter. To compare the effect of our processing, we also performed conventional boundary construction and measurements using the watershed segmentation and the line intercept method.

Methods

1. Material preparation

The bioceramic preparation process was similar to those described in previous studies [1,2]. Slurry was prepared, mixed with distilled water, silica powder (with a size of about $2\ \mu\text{m}$), and additives, sodium lauryl sulfate as a surfactant, sodium hexametaphosphate as a dispersion agent, and epoxy as a hardening agent. Bubbles were generated from the interior of the slurry by mechanical agitation over 30 min. As a result, many of the bubbles were dispersed with a high stability in the slurry and became solidified. Then, the slurry with the bubbles was dried at 50°C to come to the green body state (the drying temperature was selected to gently evaporate the water inside the slurry). The bulk green body was cut and became small pieces of cubic shape, followed by sintering at

1200°C. The resultant bioceramic foam had planar surfaces and a high cell volume fraction (porosity over 70%), high degree of interconnection between cells, variable cell sizes, and depths. As previously mentioned, the sample was not pre-treated before analysis, but solely used image analysis techniques.

2. Image analysis procedure

In general, an image analysis system consists of an image processing software and a video camera connected to an optical microscope and computer hardware. Our image analysis procedure was divided into many sub-processes: image acquisition (or capture), image preprocessing: for noise reduction to obtain a clear view of the acquired image, image segmentation: for locating and detecting the objects of interest, and image measurement. Among all these sub-processes, the image segmentation process was the most important and difficult step in ensuring quantitative characterization. To find the optimal segmentation algorithm, suitable data analysis must be carried out to understand the unique pattern of an object to be segmented compared with any other patterns. The image processing procedure is discussed in the following lines.

2.1 Image acquisition

The images of the bioceramic foam sample obtained using an optical microscope coupled to a CCD camera (HiRox) were digitized and stored in 100 dpi with 256 gray levels and 640×480 pixels. The software used for this study was Image-Pro Plus 4.0 (Media Cybernetics, MD, USA), which is a commercial software that can perform various image operating procedures automatically. Each pixel is given a light intensity value between zero to 255 in the gray scale level. The number of pixels in the image is presented as a light intensity histogram as a function of the light intensity value. We also acquired background images to regularize the intensity of the sample image.

2.2 Image preprocessing

Through image preprocessing, the image was enhanced to be pleasing to the human eye and reduce the unwanted distortion because of optical noise. The preprocessing treatment consisted of a background correction and a noise reduction step. The background correction enabled the background intensity of the overall image to be more regular. Gauss filtering, using a 7×7 pixel filter, was performed to reduce the

unspecified variance of the light intensity profile to increase image smoothness.

2.3 Operation for image segmentation

We used the morphological operations required for the image segmentation process involving thresholding, a distance function, skeletonization, and a binary-scale reconstruction operation. The first three operations are common and have frequently been used for image processing of various kinds of structures [8-11]. The threshold operation is the simplest segmentation method; it divides a gray image into a binary image on the basis of a threshold value based on light intensity [8-11]. Usually, white is used for describing the objects of interest, and black for those in the background. The threshold operations are presented mathematically in the domain set D_I as follows:

$$T_k(I) = \{p \in D_I \mid I(p) \geq k\} \quad (1)$$

In this equation, k is a threshold value, I is a gray scale image, and p is a pixel included in the image I . $I(p)$ represents a functional form of the light intensity of a pixel p .

The morphological operations begin on the basis of the concept of a structural element. The element is usually regarded as characteristic sets comprised of some small number of pixels with certain light intensities arranged in a certain pattern. Each structural element may have a different pattern, but an important common feature is that each element is used so as to make all objects of interest in an image transform step by step. In general, in a gray image (J), all objects with brighter intensity can be dilated to a small extent by adding the structural element (E) to the boundary of the objects; this operation is called dilation ($J \oplus E$).

A distance function was used in the binary image in which color was transformed to gray levels. As the distance of a pixel in the white object increased from the background objects of black color, the brightness of the pixel became higher. In addition, the skeleton operation ($S(I)$) was a useful tool for image segmentation operations; it reduced the selected objects to line segments. The other tool for segmenting an image was binary-scale reconstruction. Binary-scale reconstruction was used to present only those objects containing selected images for those and removed other images [8,12,13].

In this study, binary scale reconstruction was used to extract the marker (J) from the mask image (I), as follows:

$$\rho_I(J) = \lim_{n \rightarrow \infty} \delta_I^{(n)}(J) \quad \text{when } n \rightarrow \infty \text{ or a very large number, } (2)$$

$\delta_J^{(1)}(J)$ is called a geodesic dilation, and

$$\delta_J^{(1)}(J) = (J \oplus E) \wedge I \quad (3)$$

In this equation, the symbol \wedge stands for the point wise minimum. This study performed it to remove defects.

Conventionally, the watershed segmentation method is frequently used to break weakly connected objects such as throats between voids [8]. This method assumes the two connected objects as mountains on a map so that a geometrical boundary between the objects may discriminate the objects as the way that a river divides the two mountains. However, we used gray scale reconstruction to identify the local minima or maxima in the brightness intensity profile, and to mark cells more effectively. Fig. 2 gives a schematic presentation of these reconstruction procedures. Details on the binary or gray scale reconstruction technique are presented in the earlier studies [9,12,13].

2.4 Preparing the cell markers

First, the sample image was converted to a binary image to present cell regions in white color. It was difficult to determine the number of pixels allotted to cell regions; however, in this study, regions of white color were considered top solid struts, or otherwise, cell regions, based on the porosity of the cellular bioceramic sample. For example, if cellular bioceramic foam has a porosity value of 80%, the area percentage of white regions would be allotted as 20% and these would be considered to be regions of top solid strut. The generated top solid struts were regarded as boundaries for sure. Next, the image with the extracted boundaries was inverted into a binary image so that they are in black color. Then, the image was transformed using the distance function. The resultant image was a gray scale image such that the brightness increases with increasing distance from the background objects. These points were where the intensity was greater than other neighboring points—local maximum points. The local minimum points could be detected easily using gray scale reconstruction method: the method is depicted in Fig. 3. We assumed that all the local minimum points were cell markers, called primary cell markers in this study. This is because additional cell markers should sometimes be generated by threshold operations based on threshold values, called initial threshold values in this study. For example, if the initial threshold value is taken to be 100, the darker regions with a threshold value less than 100 are all included in the cell regions as well as primary cell markers. More detail on procedures for generating the prima-

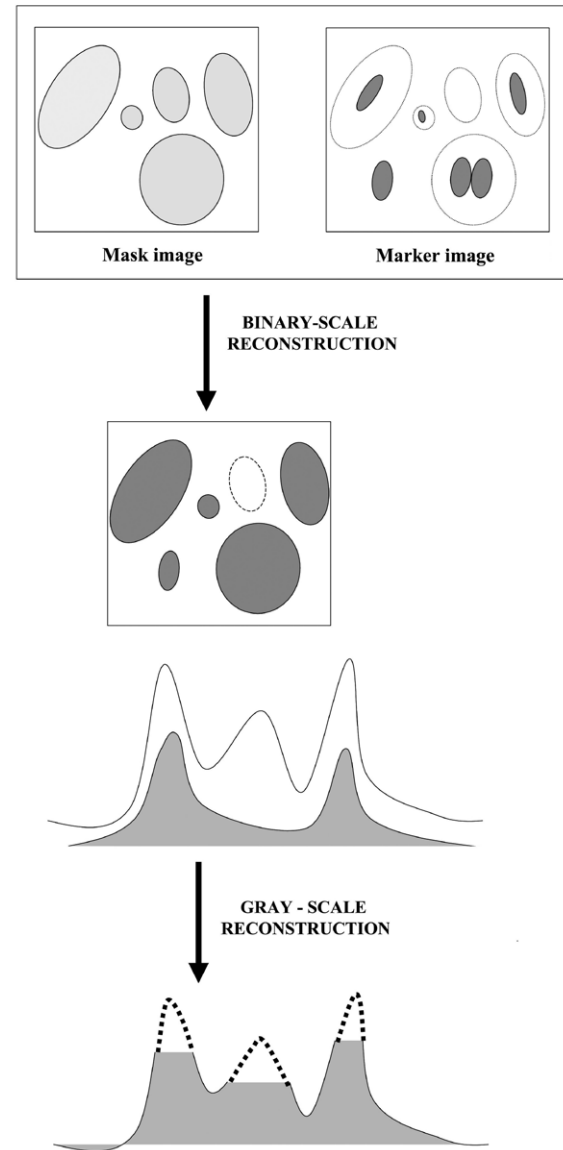


Fig. 2. The principal image operations used in this study: binary scale reconstruction (top) and gray-scale reconstruction (bottom).

ry markers can be found in the literature [12].

2.5 Automatic boundary construction

The other boundaries were generated by repetitive operations that consisted of thresholding of the sample image, its skeletonization, defect removal with the cell marker image, and image overlay of the resultant image onto the sample image. Brightness values for thresholding were between zero and the value used to extract boundaries for marking cells. For example, if certain features can be discriminated from the sample image by thresholding at a brightness value of k , they are colored as white ($T_k(I)$), and are reduced into line objects

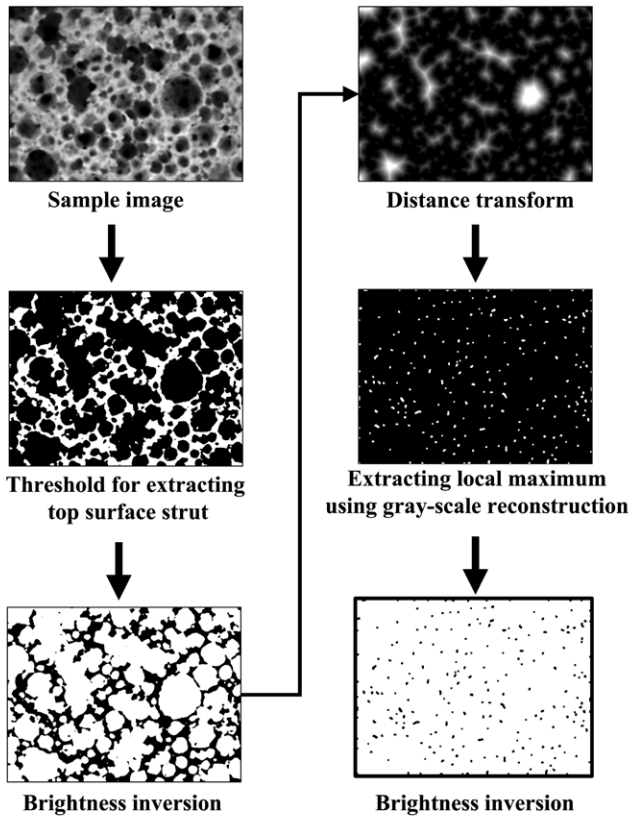


Fig. 3. The sub-process to generate the primary cell marker image. The brightness or the size of objects of interest is slightly manipulated to enhance visualization.

by a skeleton operation ($S(T_k(I))$). Then the image with the skeletonized objects was overlapped onto the sample image. Then, the threshold was applied with the overlapped image using the value of $k + 1$, and skeletonization was performed again. In a similar manner, at every threshold step, the line objects were generated gradually. A portion of the lines contributed to shape the geometrically closed objects and the other portion of the lines were merely branches or small points. These operations can be described as follows:

$$B_k(I) = S(S(T_k(I)) + T_{k+1}(I)) \quad (4)$$

$B_k(I)$ stands for the intermediate boundary construction step presented above. As these steps continued, for example at a $B_m(I)$ step ($m > k$), if some skeletonized lines are included in a threshold at the next step $T_{m+1}(I)$, then they are removed and regenerated at a $B_{m+1}(I)$ step. As $(m + 1)$ is greater than m , one can recognize as if the lines are moving to the brighter regions with an increase in the number of the steps. On the other hand, other lines, which are not included in the $T_{m+1}(I)$, remain in the image and many closed objects are generated.

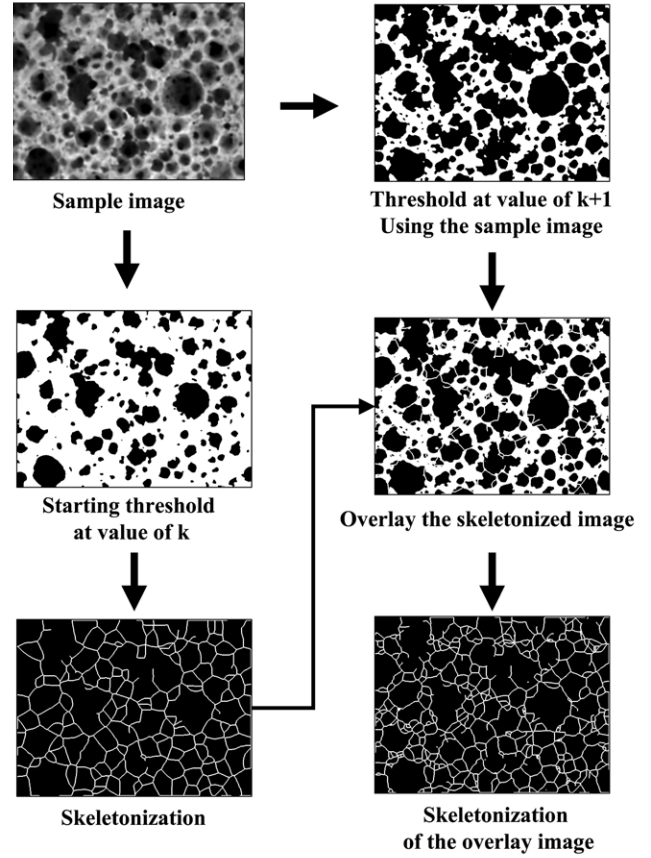


Fig. 4. The sub-process to describe the boundaries with increasing threshold values. The brightness or the size of objects of interest is slightly manipulated to enhance visualization.

The procedure is illustrated in Fig. 4.

Though many closed objects can be considered as segmented cells, not all are, because the closed shape can be generated under many conditions that are not related to cell detection. This phenomenon, called over-segmentation [9,12], was corrected using appropriate feature markers such as the cell markers (C) that were already produced.

A binary-scale reconstruction was useful in selecting only the closed objects including the cell markers. For example, in the $B_k(I)$ step,

$$Bc_k(I) = S(\rho'_{Bk(I)}(C)) \quad (5)$$

$Bc_k(I)$ is a revised boundary construction step involving removing faults that occurred in the $B_k(I)$ step; ρ' stands for the inversed boundary reconstruction operation because the cells are presented in the color black. Similarly, at the $B_{m+1}(I)$ step,

$$Bc_{m+1}(I) = S(\rho'_{Bcm(I)}(C)) \quad (6)$$

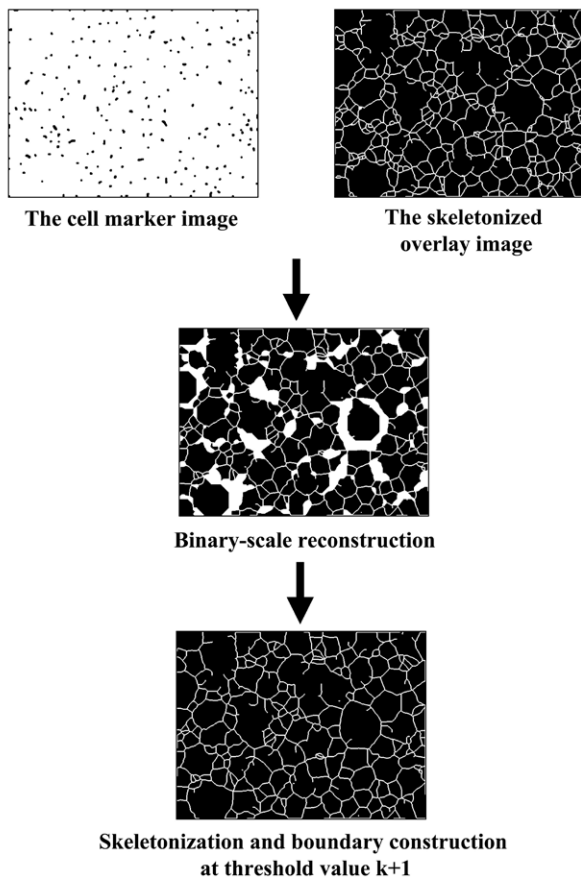


Fig. 5. The sub-process to remove the additional closed objects caused by over-segmentation using binary-scale reconstruction. The brightness or the size of objects of interest is slightly manipulated to enhance visualization.

Fig. 5 illustrates the abovementioned procedure in detail. In addition, to compare the results obtained from the newly proposed procedures described above with those of the conventional methods, we performed cell segmentation and measurements using watershed segmentation [11,12] and line intercept methods [8], respectively. The line segments were produced by breaking horizontal or vertical bars at the boundaries and selecting the lines placed on the cell regions within a spacing of 20 pixels between the bars. Then, the lengths of the selected line segments were measured.

Results and Discussion

The result of the image segmentation is shown in Fig. 6. Fig. 7 presents some images resulting from the application of the proposed procedures. The boundaries are constructed with various starting values of threshold light intensities of 60, 76,

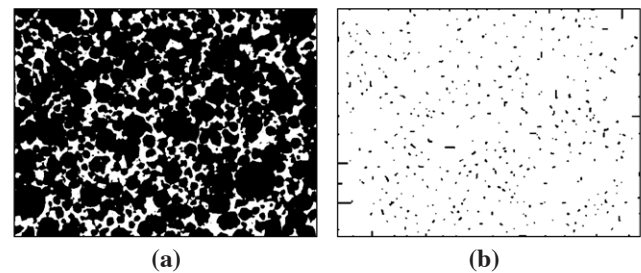


Fig. 6. The top surface strut (white) image (a) and the cell marker (black) image resulted from the sub-process presented in Fig. 3(b) : 640 pixels \times 480 pixels, and about 107 pixels equal to 1 mm.

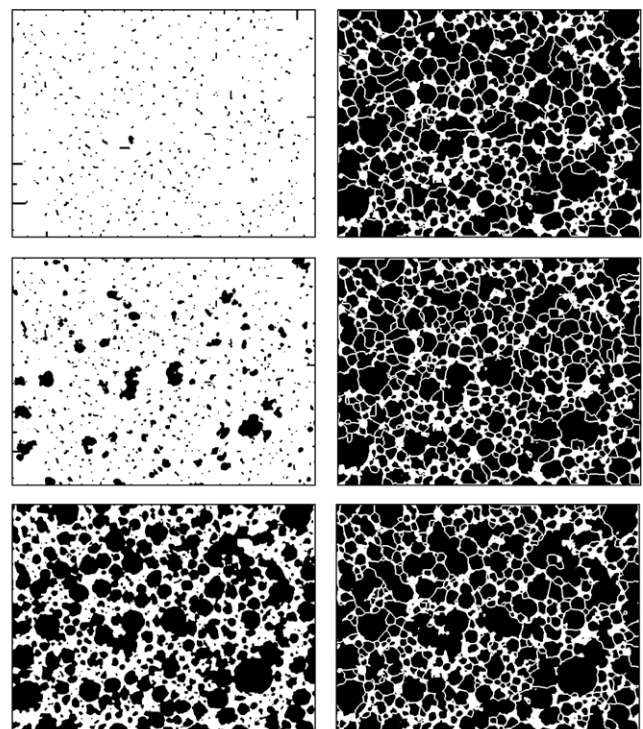


Fig. 7. The revised cell marker images (black) by including the low brightness regions to the primary marker image in Fig. 7 (left) and resultant images by adding strut image in Fig. 7 together with constructed boundaries (white) by sub-processes presented in Fig. 5 and Fig. 6 (right) : 640 pixels \times 480 pixels, and about 107 pixels equal to 1 mm.

92, 108, 116, and 124, for the secondary cell-marking process. However, in this figure, the images of only three out of six threshold values are presented (60, 92, and 116). Fig. 8 shows various measured estimation results. Fig. 8(a) presents the total number of cells produced using each method. In the figure, numbers 1~6 represent our methods with initial threshold values of 60, 76, 92, 108, 116, and 124, respectively. Numbers 7 represents the results obtained by the watershed segmenta-

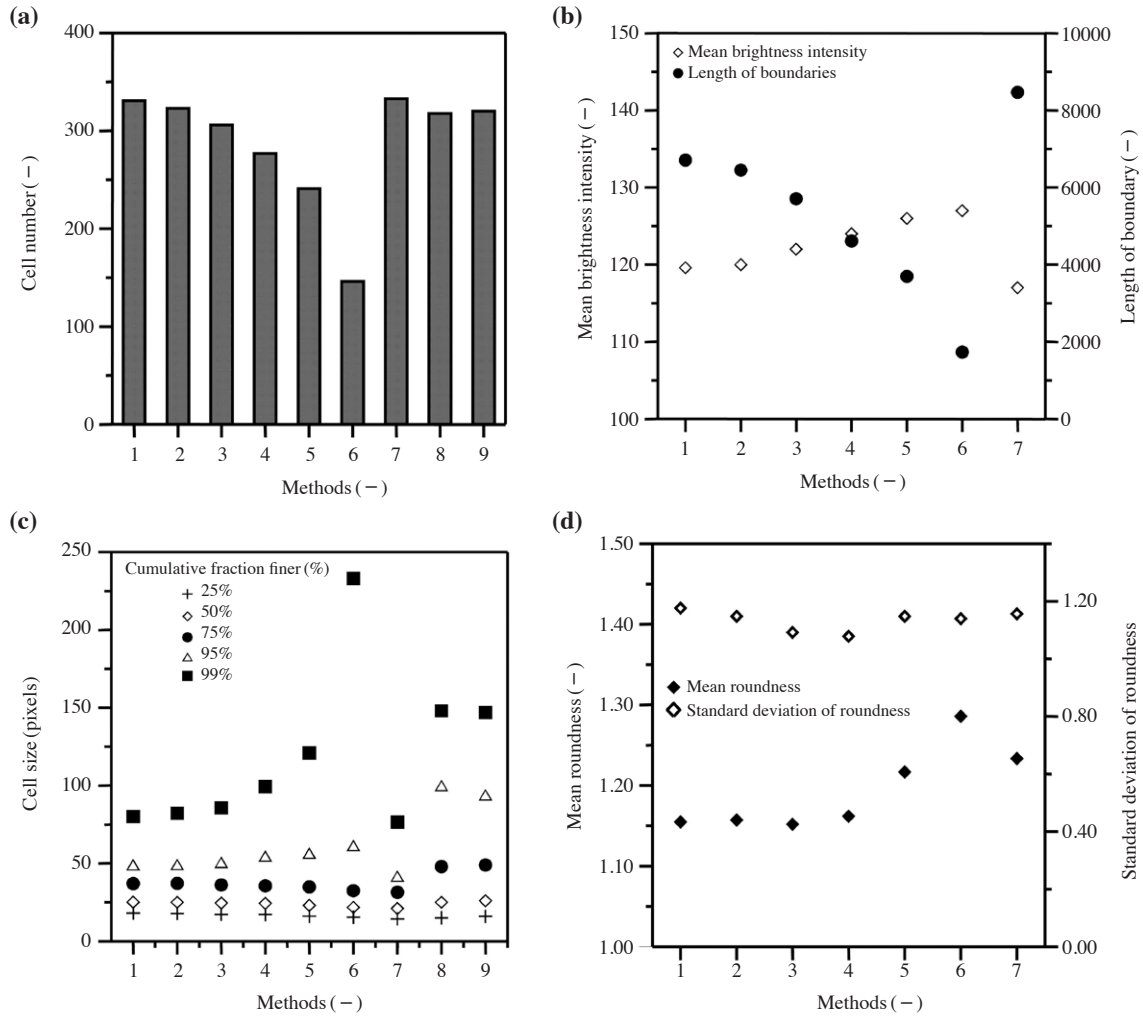


Fig. 8. (a) Total number of the cells produced by various segmentation or measurement methods; (b) Average brightness intensity values and total length of boundaries constructed by various methods; (c) Comparison of cell size at the cumulative fraction of 25%, 50%, 75%, 95%, and 99%; (d) Average and standard deviation values of the cell roundness.

tion method, and numbers 8 and 9 are produced by measuring the resultant image using the horizontal and vertical line intercept procedures without any boundary construction. On the other hand, numbers 1~7 estimate the cell size with mean diameter measurement using the automatic computer software (Image Pro plus 4.0, Cybernetics Ltd.) after the boundary construction.

Fig. 8(b) presents the mean brightness intensity value of the overlapped images. We compared the positions of the constructed boundaries produced by our method with those of the watershed segmentation method. In the image, the boundaries can be discriminated from the neighboring points through the higher brightness intensity. Consequently, the boundaries can be estimated by locating points with higher light intensity.

Therefore, we investigate the mean brightness value of the pixels in the sample image whose placement corresponds to the boundaries. This has another significant implication in that the difference of boundary placement can determine a possibility of application of secondary marking process, which is introduced above as a cell marking method by the threshold operation. The secondary marking process is used for complementation of the primary cell marking process, because the primary cell marking includes a defect due to its response only to the strut shape, regardless of the light intensity levels in the cell region. Even though there is a patent clue that can be regarded as a boundary detected by change of intensity level using human vision, it is impossible to detect that with the primary marking process alone. Hence, the addition of the

secondary marking process is useful to produce a more satisfactory discrimination between cells. For a proper application of the secondary marking process, the boundary must be placed very clearly to the gray intensity leveling, because this marking uses the threshold operation. In contrast, the watershed segmentation method cannot accept the application of this process, because it cannot consider any levels of light intensity.

Fig. 8(c) shows the cell sizes, with the cumulative fraction values of 25%, 50%, 75%, 95%, and 99%. The cell size is considered as equal to the mean diameter of each cell which can be measured by the automatic computer software. We set the minimum size of the cell as the pixel distance value of 7, which is the range of the Gauss filter matrix (7×7) used for preprocessing. The resultant cell distribution by our procedures can be estimated relative to other conventional methods [8,11,12]. The cell sizes at certain cumulative fractions are presented in the graph; the fractions of 25%, 50%, 75%, 95%, and 99% shown in the legend box. The numbers below the horizontal axis in the graph represent the measuring or segmentation tools as shown in the figure. Comparing the resultant distributions of the cell size, we find a significant difference between the measured cell sizes in the high fraction range. This is because the irregular shape of the top solid strut causes the watershed segmentation program to generate many false boundaries. The other reason is that the large cellular regions, highly interconnected with each other, produce long line segments that could be broken into two or more segments if boundaries are constructed between cells by watershed segmentation.

In our proposed method, an increase in the initial threshold results in a decrease in the total number of cells, and an increase the measured cell sizes in the high fraction range. The reason for this is that the number of cell markers is decreased when some primary cell markers are generated by the distance transform and gray scale reconstruction; these are included in the region below the initial threshold value in the sample image. This can lead to a decrease in the number of cells with high initial threshold values. However, it can be observed that, with an increase in the initial threshold value, cells of large size reduce in number, but increase in size, because the cell regions below the initial threshold values do not require boundary construction. Consequently, at high initial threshold values, one can expect that a few huge cells would occur. This is supported by Fig. 8(c), which shows the larger cell sizes in the fraction value range higher than 75%.

Here, in the relatively lower range, the cell sizes become smaller with increase in the initial threshold values.

In the watershed segmentation (number 7), cell sizes are smaller than measured by our procedures. This is probably because watershed segmentation constructs the boundaries based on the shape of the background image [11,12], the top solid struts in this study, and, therefore, an irregular background can give rise to lots of boundaries, often redundantly. The results of the line intercept method (number 8 and 9) shows that the measured sizes are about equal to or greater than those from our method, especially the size corresponding to 75%. This is caused by the highly interconnected cell regions that could otherwise be divided into two or more cellular objects.

Fig. 8(d) shows the average and standard deviation values of the roundness of the cells against their corresponding cell size. Because the roundness of a circular feature is unity, how close the average values are statistically to unity is equal to how close the shapes of cells are to circles as a whole. This figure shows that the values of roundness of the cells for our method are slightly closer to unity than for watershed segmentation. This proves that, using our method, the boundaries of cells are shaped successfully as round-type which is similar to typical foam. With low and high initial threshold values, the shape of cells deviates from a homogeneous round shape. The reason for this is that, within the low threshold values, the regions are so highly segmented that this generates many small cells whose roundness values are considerably sensitive to change of pixel placement, and within the high initial threshold values, the cell markers occupy a considerable portion of the image so that the cells are not suitably segmented. With the standard deviation values, we attempt to estimate statistically the homogeneity of the shape of cells. This can be determined and shows that the cells are more homogeneous in shape at lower threshold values. In Fig. 8(d), in general, the estimated cells are more homogeneous using our methods than the watershed segmentation method. Given the appropriate cell-marking, the boundary construction can be more accurate in terms of brightness intensity as well as the shape of the background image.

Conclusion

A new image processing algorithm to analyze the cellular structure of bioceramic foams consists of four steps, including

image acquisition, preprocessing, segmentation, and measurement, was proposed. The image segmentation step is comprised of the cell marking and cell boundary construction processes. The cell marking process is further divided into primary and secondary sub-processes. After top surface solid regions are extracted from the image of the bioceramic foam surface, the cells are marked based on their shapes and spatial distribution in the image; this is the primary cell marking. In addition, the secondary sub-process considers the light intensity levels using the threshold operation. Then, skeletonized boundaries are constructed.

In contrast, the conventional processing (i.e., the watershed segmentation process) makes it impossible to apply that, because the operation can regard only the geometrical shape of objects and the background in an image, neglecting the light intensity of objects. Therefore, a boundary construction operation can describe the skeletonized boundaries based not only on the cell shapes, but also the light intensity of the cells. The effectiveness of the proposed reconstruction method is compared with the earlier methods, the result of the watershed segmentation method and, as for the cell size distribution measurement, with that of the line interception method. The advantage of the proposed construction method over the watershed segmentation lies in recognition of the light intensity as well as the strut shape. This can be useful to process or manipulate any segmented cell object using the light intensity properties.

Then, we measure the total number of cells, the mean cell diameter, the total length of the constructed boundaries and their corresponding light intensity in the sample image distribution. As a result, we discovered that, up to cumulative distribution of 50%, the corresponding cell size is similar regardless of the process applied. However, over a cumulative distribution of 75%, a larger deviation between our method and the other methods is observed, which is attributed to a coalescence of mid-sized cells that form larger cells on increasing the threshold value in secondary marking.

Nomenclature

Roman

$B_X(Y)$: an intermediate boundary construction step in an image Y, with threshold value X and X + 1.
 $B_{cX}(Y)$: a revised boundary construction step involving

removing faults that occurred in the $B_X(Y)$ step

D_X : domain set of image X,
 E : structural element
 I, J, C : gray scale images
 k : a threshold value
 p : a pixel included in the image.
 $S(X)$: skeleton operation of image X.
 $T_X(Y)$: threshold operation of image Y based on the threshold value of X.

Greek

$\delta_X^{(r)}(Y)$: the geodesic dilation r times
 $\rho_X(Y)$: the binary scale reconstruction to extract the marker (Y) from the mask image (X)
 $\rho'_X(Y)$: the inversed boundary re-construction operation

References

1. Montanaro L, Jorand Y, Fantozzi G, Negro A. Ceramic foam by powder processing. *J Eur Ceram Soc* 1998;18:1339-1350.
2. Sepulveda P, Binner JGB. Processing of cellular ceramics by foaming and in-situ polymerization of organic monomers. *J Eur Ceram Soc* 1999;19:2059-2066.
3. Hammel EC, Idhodaro OLR, Okoli OI. Processing and properties of advanced porous ceramics: An application based review. *Ceram Int* 2014;40:15351-15370.
4. Uhlířová T, Gregorová W, Necina V. Preparation of cellular alumina ceramics via biological foaming with yeast and its microstructural characterization via stereological relations, *J Eur Ceram Soc* 2015;35:187-196.
5. Tong M, Cole K, Brito-Parada PR, Neethling S, Cilliers JJ, Banford AW, et al. Geometry and topology of two-dimensional dry foams: computer simulation and experimental characterization. *Langmuir* 2017;33:3839-3846.
6. Ou X, Zhang X, Lowe T, Blanc R, Rad MN, Wang Y, et al. X-ray micro computed tomography characterization of cellular SiC foams for their applications in chemical engineering. *Mater Charact* 2017;123:20-28.
7. de Pascalis F, Nacucchi M, Scatto M, Albertoni R. Quantitative characterization of low-density, high performance polymeric foams using high resolution X-ray computed tomography and laser confocal microscopy, *NDT E Int* 2016;83:123-133.
8. Kurzydowski KJ, Ralph B. The quantitative description of the microstructure of materials. Boca Raton: CRC Press; 1995.
9. Sonka M, Hlavac V, Boyle R. Image processing, analysis and machine vision. 3rd ed. Boston: PWS; 2007.
10. Pratt WK. Digital image processing 4th ed. Hoboken: Wiley-Interscience Publisher; 2006.

11. Russ JC, Neal FB. The Image processing handbook 7th ed. Boca Raton: CRC Press; 2016.
12. Vincent L. Morphological gray scale reconstruction in image analysis: applications and efficient algorithms. IEEE Trans Image Process 1993;2:176-201.
13. Aminzadeh M. A machine vision system for in-situ quality inspection in metal powder-bed additive manufacturing. Ph.D dissertation, Georgia Institute of Technology; 2016.